




Graphene aerogel induced by ethanol-assisted method for excellent electromagnetic wave absorption

Shuangqiang Shi¹, Sue Ren^{1,*}, Sijia Hao^{1,2}, Yubin Chen^{1,2}, Cheng Yang^{1,2,*} , and Shenglong Dai¹

¹Research Center of Graphene Applications, Beijing Institute of Aeronautical Materials, Beijing 100095, People's Republic of China

²Beijing Institute of Graphene Technology, Beijing 100094, People's Republic of China

Received: 28 April 2021

Accepted: 19 August 2021

Published online:
3 January 2022

© The Author(s), under exclusive licence to Springer Science+Business Media, LLC, part of Springer Nature 2021

ABSTRACT

Graphene aerogels with three-dimensional network structure exhibit excellent electromagnetic (EM) wave attenuation capacity and are often designed as EM-absorbing materials. However, the fabrication processes of these materials are generally sophisticated and time-consuming. Herein, a series of graphene aerogels are synthesized successfully through a simple modified hydrothermal method using ethanol and water as the solvent. The effects of the volume ratio of ethanol-to-water (EtOH/H₂O) on the chemical compositions, microstructures, and EM absorption properties of the aerogels are investigated. Results demonstrate that the microstructure and EM-absorbing ability are strongly dependent on the volume ratio of EtOH/H₂O, and the best performance is obtained with EtOH/H₂O of 1:1. Owing to the optimized ratio, the aerogel with 4.1 mg/ml exhibits a remarkable minimum reflection loss of – 52.6 dB and a broad efficient absorption bandwidth of 7.65 GHz under an ultralow filler content (3 wt%), showing obvious advantages compared with most graphene-based absorbers. This work reveals that the graphene aerogel prepared through this ethanol-assisted hydrothermal protocol is a promising candidate for lightweight and economical EM absorption material.

Introduction

With the large-scale popularization of electronic equipment, electromagnetic (EM) wave pollution becomes a nonnegligible and severe issue nowadays. The EM wave pollution gives rise to serious harm to

both the highly sensitive precision electronic equipment and the health of human beings [1, 2]. The use of electromagnetic wave-absorbing materials (EAMs) is proven to be an effective method to eliminate EM wave pollution significantly, receiving considerable attention in the civil and military fields. The ideal EAMs are supposed to possess lightweight, strong

Handling Editor: Joshua Tong.

Address correspondence to E-mail: sue_ren@bit.edu.cn; chengyang_78@126.com

<https://doi.org/10.1007/s10853-021-06461-5>

absorption ability, broad absorption bandwidth, and thin matching thickness, which are urgent requirements of new era [3, 4]. Generally, the traditional EAMs such as ferrites, metallic magnets powder, and ceramic exhibit superior EM wave absorption performance. However, their shortcomings are obvious, such as poor impedance matching, narrow effective absorption bandwidth (EAB), high bulk density, low corrosion resistance [5], which seriously restrict their applications in aerospace, aviation, and electronic communication fields.

Carbon-based materials exhibit high thermal stability, good corrosion resistance, high conductivity, and unique dielectric properties [6], which are regarded as promising candidates for traditional EAMs. As a 2D carbon-based material, graphene is often designed to meet the demands of high-performance EM attenuation materials due to its remarkable properties, such as large specific area, high thermal conductivity, and excellent electron mobility [7]. Wang et al. [8] synthesized the MoS₂/graphene composites used for EM wave absorption, and results indicated that the minimum reflection loss (RL_{\min}) value of -50.9 dB was observed at 11.68 GHz for the sample with a thickness of 2.3 mm. Besides, hybrids of graphene and γ -Fe₂O₃ nanotube [9], TiO₂ nanoparticles [10], carbon spheres [11], polyaniline [12], MXene [13, 14], Ni [15] have also been prepared and exhibited improved EM absorption ability. However, the complex synthesis procedures and high filler ratio (≥ 10 wt%) are still urgent problems to be solved. In addition, studies on pure-graphene EAMs have been reported [16, 17], but with thermal annealing at 900 °C or even higher temperatures, no significant EM absorption performance improvement is observed. Recently, macroscopic 3D graphene aerogels from 2D graphene sheets are frequently reported [18–21] because they present excellent EM absorption performance due to their interconnected network structure, which can improve the multiple reflections of the incident EM wave and lead to enhanced absorption. For instance, Bidsorkhi et al. [22] synthesized 3D porous graphene aerogel constituted by a polyvinylidene fluoride polymer matrix, which showed fine-tuned EM absorption performance, as well as thermal, mechanical, and water resistance properties. Carbon nanotube/graphene aerogel was also prepared by Lv et al. [23] and ultra-wideband EM absorption of 8.5 GHz was obtained in the 18–26.5 GHz frequency range. In addition, Zhang

et al. [18] prepared ultralight graphene aerogel by a solvothermal process and gained EAB of 60.5 GHz after compressing, which covered 93.8% of the total frequency band. However, the preparation procedures of graphene aerogels are usually accompanied by procedures like dialysis [19], differential centrifugation [18], gradient elution [18, 21], and vacuum impregnation [18–21, 23], which are sophisticated and time-consuming. In addition, the 3D structure is not very suitable for the traditional coating technique. Therefore, it is a great challenge to develop EAMs by a simple and feasible method with extraordinary EM absorption performance and widespread applications.

In this study, a graphene aerogel material with excellent EM absorption is successfully fabricated via a modified hydrothermal method, in which graphene oxide is used as the raw material and ethanol and water as the solvent. By varying the volume ratio of EtOH/H₂O, the microstructures of the graphene aerogels can be easily tuned. Their EM wave-absorbing performance in 1–18 GHz is investigated. The results indicate that the graphene aerogel with the optimized conditions shows the features of low density (4.1 mg/ml), small filling ratio (3 wt%), superior EM-absorbing performance ($RL_{\min} = -52.6$ dB), and broad absorption bandwidth (maximum EAB of 7.65 GHz). In addition, this synthetic protocol does not require ultrahigh-temperature treatment and other complicated steps. It is believed that such graphene aerogel would be a potential candidate for lightweight and economical EAM in the near future.

Experimental section

Materials

Graphene oxide (GO) was synthesized by oxidizing natural graphite flakes (32 mesh, 99.9%, Qingdao Tiansheng Graphite Co., Ltd.) in the manner of a modified Hummers method as described in reference [24]. Ethanol (EtOH, AR, Sinopharm Chemical Reagent Co., Ltd.) was used without further purification, and deionized water was employed in all procedures.

Fabrication of graphene aerogels

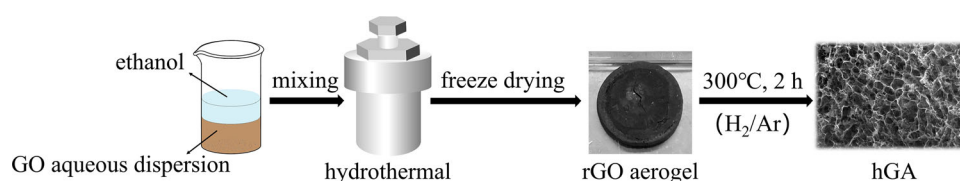
The fabrication process for graphene aerogels is demonstrated in Fig. 1. GO was dispersed in deionized water with continuous stirring and ultrasonic treatment to form a stable aqueous dispersion, in which GO was fully exfoliated. Then, ethanol was introduced into this dispersion followed by rigid stirring, resulting in a final dispersion with 5 mg/ml GO. Subsequently, the well-dispersed solution was transferred to a 200-ml Teflon-lined stainless-steel autoclave and hydrothermally assembled at 180 °C for 12 h to form the graphene-based 3D hydrogel. The hydrogel was quickly frozen using liquid nitrogen and freeze-dried to maintain the 3D monolithic architecture. Then, the obtained reduced graphene oxide (rGO) aerogel was then placed in a tube furnace and heated at 300 °C for 2 h under a flow of H₂/Ar (10/90), giving rise to heat-treated graphene aerogel (hGA). The final product from this process was a black monolithic aerogel composed of graphene networks.

Here, for investigating the influence of ethanol on the microstructure of produced graphene aerogel, the EtOH/H₂O volume ratios of GO dispersions before hydrothermal were controlled to be 6:6, 4:8, 3:9, and 0:12 (water solvent), and the corresponding hGA samples were denoted as hGA1, hGA2, hGA3, and hGAW, respectively.

Characterization and measurement

SEM images were obtained through a field-emission scanning electron microscope (FEI Nova Nano SEM 450) to characterize the cross-sectional morphology of samples. Before observed, monolithic samples were taken and sputter-coated with Pt. FT-IR spectra were recorded via a Nicolet IS10 Fourier transfer infrared spectrometer. Raman spectra were recorded on a confocal Raman spectrometer (Renishaw, inVia) with an operating wavelength at 532 nm. XPS spectra were performed using an X-ray photoelectron spectrometer (Thermo Scientific Escalab 250Xi) with monochromatic Al K α as the excitation source.

Figure 1 Schematic illustration for the preparation process of graphene aerogels.



The electrical conductivity of the samples was measured by a four-probe powder resistivity meter (ST2722-SZ, Suzhou Jingge Electronic Co., Ltd.). Four samples with the same weight were pounded into powder and placed in the loading chamber, respectively. Turn the handwheel to make the electrodes press the powder, and the resistivities of the samples under different pressures were recorded. The electromagnetic parameters were measured using the coaxial-line method on a vector network analyzer (HP-8722ES, Agilent). The fragmented hGAs (3 wt%) were mixed with melted paraffin with continual stirring. The mixtures were then transferred to the mold after cooled slightly. The test samples were obtained by pressing them into concentric rings with Φ_{in} of 3.04 mm and Φ_{out} of 7.00 mm.

Results and discussion

Digital photograph of hGAs is presented in Fig. 2a. It can be seen that the hGA1 has the largest volume, and as the ethanol used decreases, the volume of aerogels gradually shrinks. Figure 2b shows the density variation trend of graphene aerogels before and after heat treatment. Particularly, the obtained hGA1 has an ultralow density of 4.1 mg/ml, while the density of hGAW exceeds 18 mg/ml. This result should be attributed to the different degrees of shrinkage of graphene sheets.

To better understand the microstructures of the hGAs, SEM was used to observe the cross section of the samples. Figure 3a is the SEM image of GO used as the raw material, which shows a large-size of flake structure. As displayed in Fig. 3b, hGA1 shows a porous structure with pore size on the micrometer scale. The enlarged view indicates that the curled graphene sheets that make up this pore structure are rough and wrinkled (Fig. 3c), which is helpful to the EMW scattering [25]. As the ethanol decreases, graphene sheets stack and microscopic pores shrink gradually, resulting in the dense structure of the aerogels (Fig. 3d–g). The average pore sizes of hGA1,

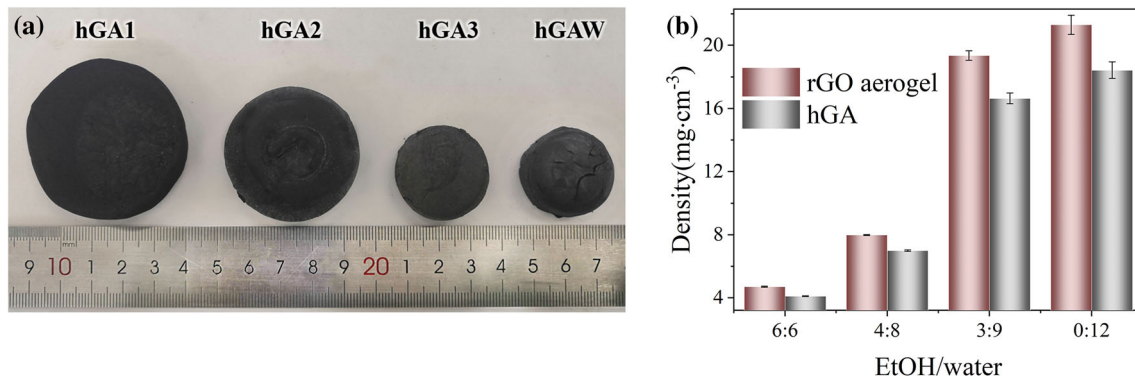


Figure 2 Digital photographs **a** and density **b** of graphene aerogels.

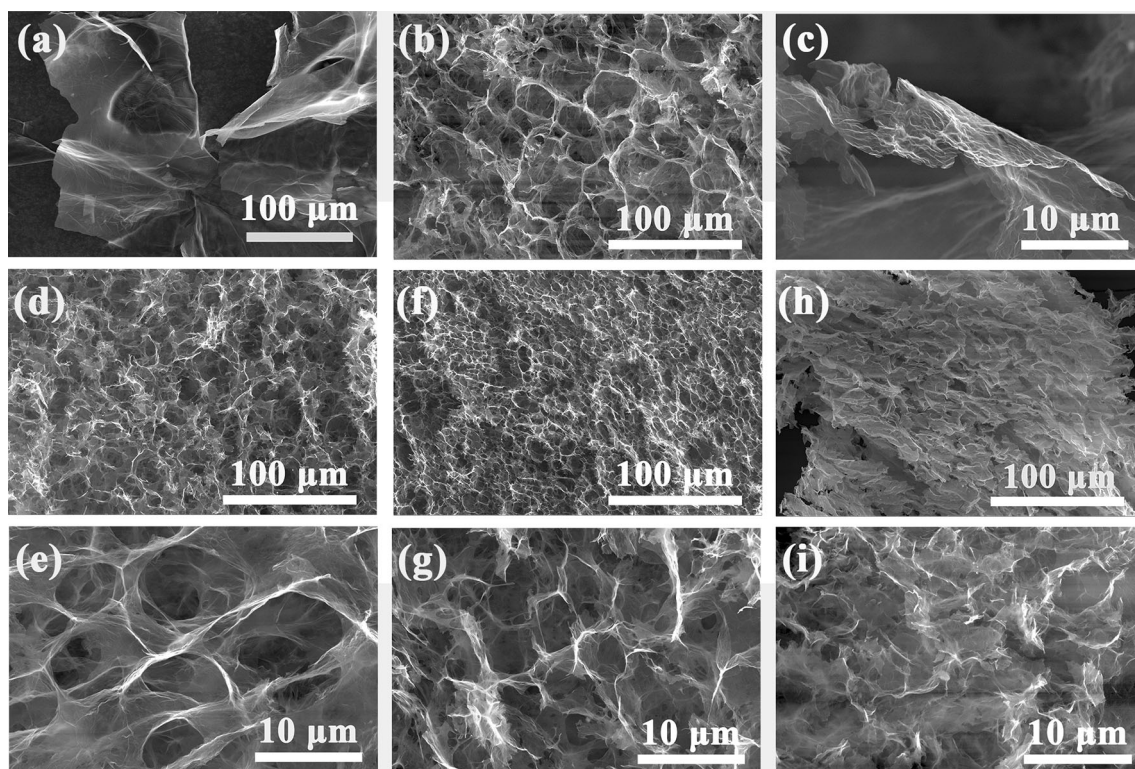


Figure 3 SEM images of cross section for **a** GO, **b, c** hGA1, **d, e** hGA2, **f, g** hGA3, and **h, i** hGAW with different magnifications.

hGA2, and hGA3 are around 23, 14, and 5 μm, respectively. However, hGAW exhibits a heterogeneous microstructure (Fig. 3h–i), where the porous structures almost disappear. The image with larger magnification shows that the graphene sheets stack badly. So it can be seen that the introduction of a suitable amount of ethanol is beneficial for the formation of porous skeleton structure [26] and can inhibit agglomeration of graphene sheets effectively during the hydrothermal process.

The results of Raman spectra could reflect detailed structure information of the hGAs. As shown in

Fig. 4, two sharp peaks assigned as D band and G band are observed around 1350 and 1590 cm^{-1} , which are related to the defects and graphitic area, respectively [17]. The intensity ratio of D band and G band (I_D/I_G) is often used to characterize the electronic conjugation state of graphene materials [27]. After being reduced, the I_D/I_G values of hGAs (about 0.9) are higher than that of GO (0.747), suggesting the increased number of sp^2 carbon domains and vacancy defects [28, 29], which is conducive to the increment of polarization centers. In addition, all hGAs show

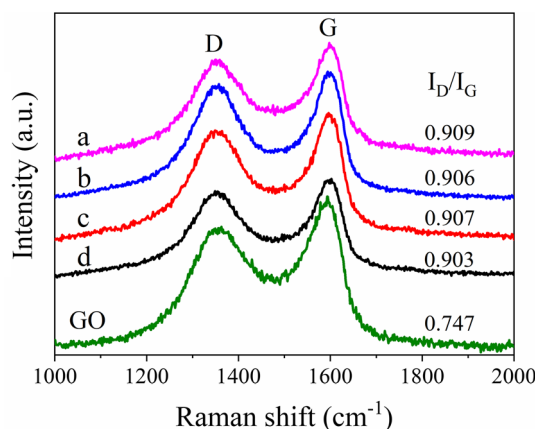


Figure 4 The Raman spectra of hGA1 **a**, hGA2 **b**, hGA3 **c**, hGAW **d**, and GO.

similar I_D/I_G , revealing the fact that they have similar π -conjugated structures.

FT-IR spectra of hGAs and GO are shown in Fig. 5. The characteristic peaks at 1737, 1626, 1391, and 1099 cm^{-1} of GO are assigned to the C=O stretching vibration, C=C stretching vibration of the benzene ring, C–H bending vibration, and C–O–C stretching vibration, respectively. In addition, the broad peak located around 3400 cm^{-1} is the stretching vibration of O–H, which is mainly contributed by the adsorbed water [30]. After the hydrothermal treatment, the peak of O–H almost disappears due to the hydrophobic property of hGAs. The peak intensity of other oxygen-containing functional groups is also weakened heavily because of the reduction procedures. But there still have several obvious peaks in the FT-IR spectra of hGAs. The peaks at 1223 and 1737 cm^{-1} are stretching vibration of C–OH and

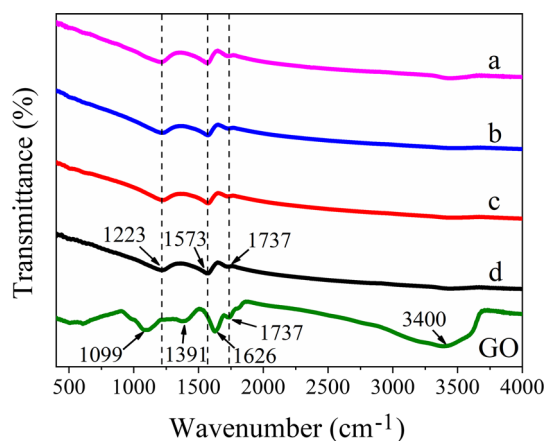


Figure 5 The FT-IR spectra of hGA1 **a**, hGA2 **b**, hGA3 **c**, hGAW **d**, and GO.

C=O, and the peak at 1573 cm^{-1} corresponds to C=C stretching vibration of the benzene ring. FT-IR result indicates the incomplete reduction of hGAs.

The surface chemical changes of hGAs and GO are characterized by XPS and the results are presented in Fig. 6. In Fig. 6a, all the samples exhibit two distinct peaks of C 1s and O 1s, and the relative intensity of C 1s increases for hGAs, suggesting the effective reduction of GO. Furthermore, the C 1s spectra can be deconvoluted into four carbon species in different binding states, including C–C/C=C, C–OH, C–O–C, and C=O. As shown in Fig. 6b–f, the area of C–C/C=C increases from 22.64% (GO) to about 36% (hGAs), confirming the reduction of GO again. But there still have some oxygen-containing groups in hGAs, which is consistent with the FT-IR analysis, and these residual groups will contribute to the increase in polarization loss [21]. At the same time, the approximate area of oxygen-free group indicates a similar reduction degree of all hGAs.

Graphene hydrogels prepared by the traditional hydrothermal method usually undergo significant volume shrinkage, as shown in Fig. 2a. This is because the hydrothermal process is often accompanied by the reduction reaction that will transform hydrophilic GO into hydrophobic rGO. The loss of oxygen-containing functional groups leads to reduced interlamellar repulsion and restoration of the conjugated structure, and the increased π – π interactions between adjacent flakes will trigger the gelation process. However, due to the high surface tension of water, graphene sheets of rGO are highly curled, resulting in enormous clumping and volume shrinkage of hydrogels during the process [21]. Ethanol has relatively low surface tension, and replacing part of water with ethanol can reduce the surface tension of the solvent and help inhibit the shrinkage of hydrogels to some extent [31]. However, it is difficult for GO to be thoroughly exfoliated in anhydrous ethanol [32], and when too much ethanol is added into GO aqueous solution, precipitation of agglomerated GO sheets will be observed. Some researchers have used methods like differential centrifugation [18] or extending ultrasonic time [33, 34] to get homogeneous GO/ethanol dispersions, which are time-consuming and hard for mass production. In addition, the gradient elution method is also required to replace ethanol with water to facilitate the following freeze drying [18, 21, 30], which will further increase the preparation cost. Therefore, the use of

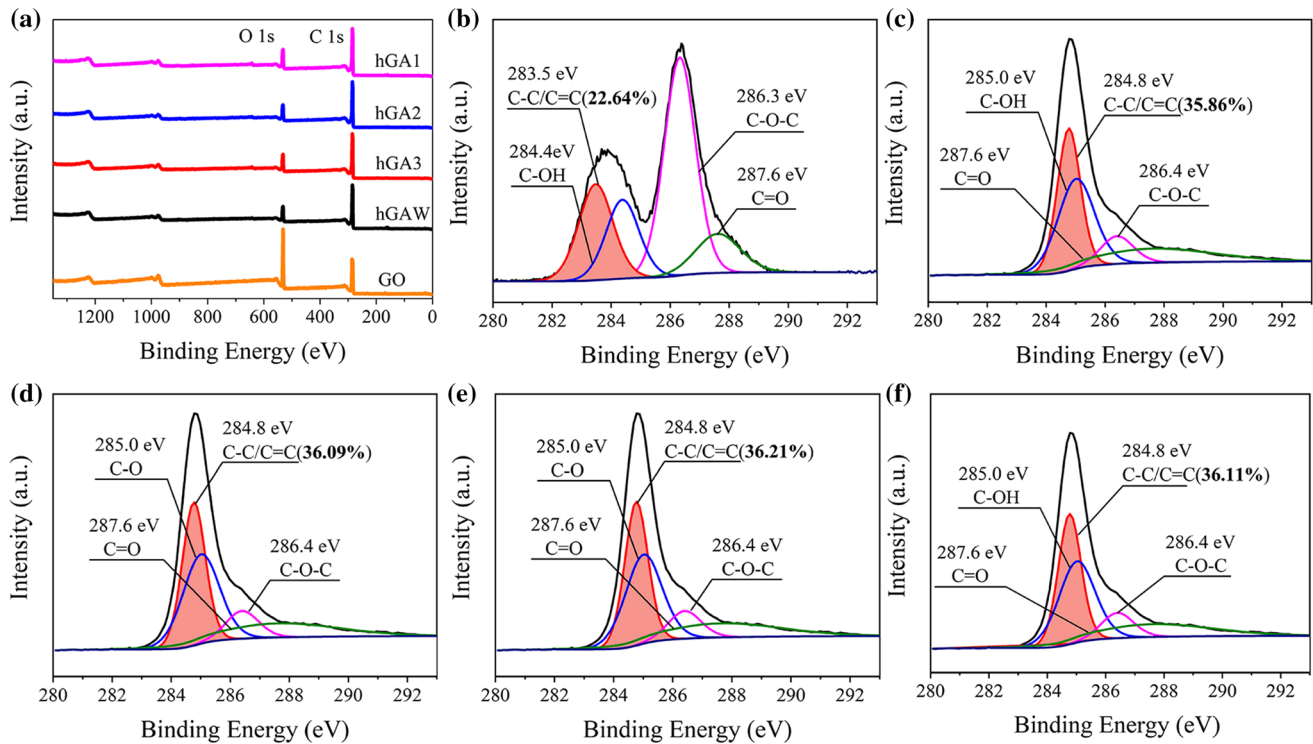


Figure 6 a The XPS spectra of hGA1, hGA2, hGA3, hGAW, and GO. b–f High resolution of C1s XPS spectra of GO, hGA1, hGA2, hGA3, and hGAW.

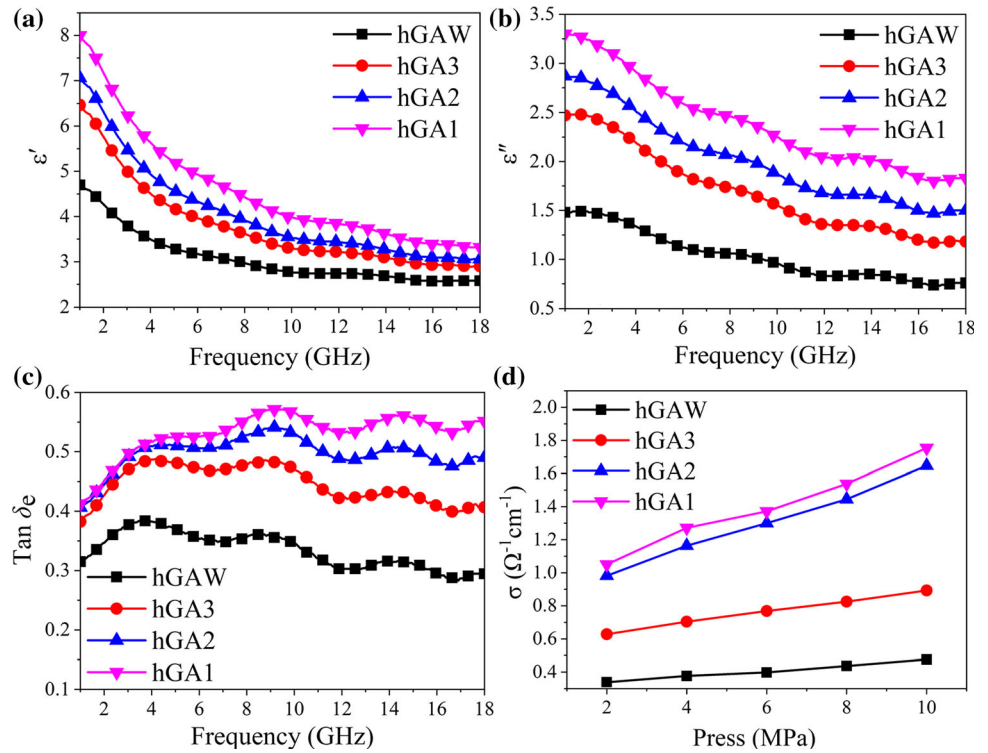
EtOH/H₂O mixed solution is a relatively economical and practical method.

Coaxial-line method was used to test the electromagnetic parameters of hGA/paraffin composites with 3 wt% filling ratio. The real parts (ϵ') and imaginary parts (ϵ'') of relative complex permittivity ($\epsilon_r = \epsilon' - j\epsilon''$) and dielectric loss tangent ($\tan \delta_e = \epsilon''/\epsilon'$) of the hGAs with different EtOH/H₂O ratios are shown in Fig. 7. As to the relative complex permeability ($\mu_r = \mu' - j\mu''$), because there are no magnetic components in hGAs, it can be regarded as 1.

It can be seen from Fig. 7a–b that the permittivity values of all samples decrease as frequency increases from 1 to 18 GHz, attributing to dielectric dispersion [12]. Besides, both ϵ' and ϵ'' increase with the relative content of ethanol rising. It is well known that ϵ' and ϵ'' are associated with the ability of EAMs for energy storage and dissipation during the polarization process [35], respectively. In Fig. 7a, the ϵ' values of hGA1 are higher than those of other hGAs, demonstrating the better capability of electromagnetic energy storage in the case of hGA1. In general, the microstructure and degree of graphitization determine the complex permittivity of carbon materials [36]. Based on the SEM results, it should be ascribed

to the multiple reflection and scattering of EM wave caused by the porous structure of aerogels. Multiple reflection and scattering can change the propagation path of EM wave and extend its propagation time in the materials, thus leading to the increase in ϵ' . Meanwhile, when EM wave interacts with the graphene sheets, multiple scattering and absorption can lead to greater attenuation of electromagnetic energy, resulting in higher ϵ'' (Fig. 7b). In addition, as the concentration of ethanol increases, the density of the hGAs decreases gradually (Fig. 2). Considering that the mass fraction of hGAs was kept consistent during the test, the volume fraction will be higher when the density is lower. Higher volume fraction can make the graphene sheets easier to contact each other in the matrix and lead to increased conductivity (Fig. 7d). According to the free electron theory [37, 38], $\epsilon'' \approx 1/\rho\omega\epsilon_0$, where ρ is the resistivity and ϵ_0 is the permittivity of vacuum. Therefore, the higher conductivity of hGAs, the higher ϵ'' value. The phenomenon that conductivity of rGO increases with ethanol concentration growing has also been discovered in Liao's work [39], which would be explained that ethanol can promote the self-assembly degree of graphene sheets,

Figure 7 Real parts **a** and imaginary parts **b** of the complex permittivity of hGAs. **c** Dielectric loss tangent of hGAs. **d** Bulk electrical conductivities of hGAs under different pressures.



and the increased free electrons result in higher conductivity.

Tan δ_e is usually used to evaluate absorbers' electromagnetic energy dissipation capacity. As shown in Fig. 7c, all samples present fluctuations in the full range of 1–18 GHz, which may suggest a resonance behavior [40, 41]. Consistent with the variation trend of ϵ' and ϵ'' , tan δ_e values are also enhanced with the increased proportion of ethanol, indicating their increased dissipation capacity to electromagnetic energy.

To describe the polarization relaxation processes, the Cole–Cole semicircle is induced. According to Debye relaxation theory [42, 43], the relationship between ϵ' and ϵ'' can be described by

$$\left(\epsilon' - \frac{\epsilon_s + \epsilon_\infty}{2}\right)^2 + (\epsilon'')^2 = \left(\frac{\epsilon_s - \epsilon_\infty}{2}\right)^2 \tag{1}$$

where ϵ_s and ϵ_∞ are static dielectric constant and optical frequency dielectric constant, respectively. The type of polarization is usually determined by Cole–Cole semicircle as each semicircle corresponds to one Debye relaxation process [16, 44]. The ϵ'' – ϵ' curves of all samples are displayed in Fig. 8. It can be seen that there are three partially overlapped semicircles for all hGAs, corresponding to multiple Debye relaxation processes, including dielectric relaxation

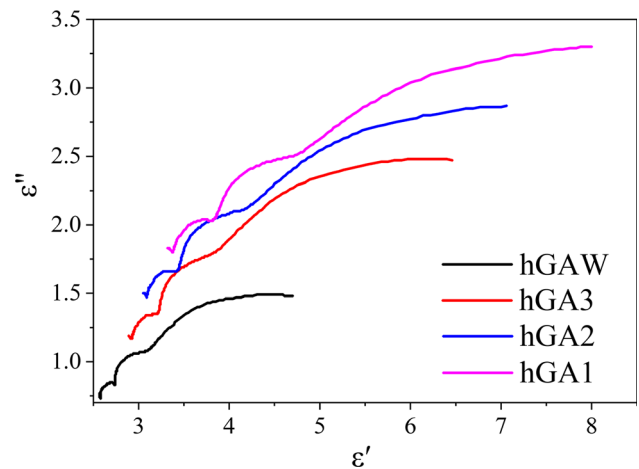


Figure 8 Cole–Cole curves of hGAs.

caused by induced charges and polarization relaxation by defects and residual groups [45]. In addition, as the concentration of ethanol increases, the line gradually moves to higher values, and the radius of the arc also increases, indicating the gradual enhancement in the contribution of the multiple Debye relaxation to permittivity [45, 46].

According to the transmission line theory, RL can be calculated according to the followed equations [7, 47]

$$RL(\text{dB}) = 20 \lg \left| \frac{Z_{\text{in}} - Z_0}{Z_{\text{in}} + Z_0} \right| \quad (2)$$

$$Z_{\text{in}} = Z_0 (\mu_r / \varepsilon_r)^{\frac{1}{2}} \tanh \left[j \left(2\pi f d (\mu_r \varepsilon_r)^{\frac{1}{2}} / c \right) \right] \quad (3)$$

where Z_0 is the impedance of the free space, Z_{in} is the input impedance of the EAMs, f is the frequency of the EM wave, d is the thickness of the EAMs, and c is the velocity of light. Figure 9 presents the calculated 3D RL values of hGAs with different thicknesses and frequencies, and the black line represents the $RL = -10$ dB. It can be seen from Fig. 9a–d that the absorption performance of hGAs improves with the concentration of ethanol increasing. When the solvent is deionized water, the corresponding aerogel hGAW

displays a poor performance and its RL could hardly reach the effective absorption value (-10 dB). As to hGA1, its RL is close to -50 dB at 4 mm. The exact values of RL_{min} and EAB are listed in Table 1. It can be seen that with ethanol increases, not only the RL_{min} of hGAs decreases gradually, the EAB also becomes broadened. As to hGA1, its EAB can reach 7.65 GHz at 3.2 mm and RL can reach -52.6 dB at 4.8 mm, as shown in Fig. 9e. Compared to previous graphene-based absorbers reported in the literature (Fig. 9f), the hGA1 in this work shows high EAB and $|RL_{\text{min}}|$ values.

It can be seen from the above data that the increased permittivity is responsible for the reduced thickness of peak absorption of the hGA/paraffin composite. According to the quarter-wavelength

Figure 9 Calculated 3D reflection loss plots with projections for **a** hGA1, **b** hGA2, **c** hGA3, and **d** hGAW. **e** Reflection loss curves for hGA1. **f** EAB and RL_{min} for the hGA1 and graphene-based absorbers in some references.

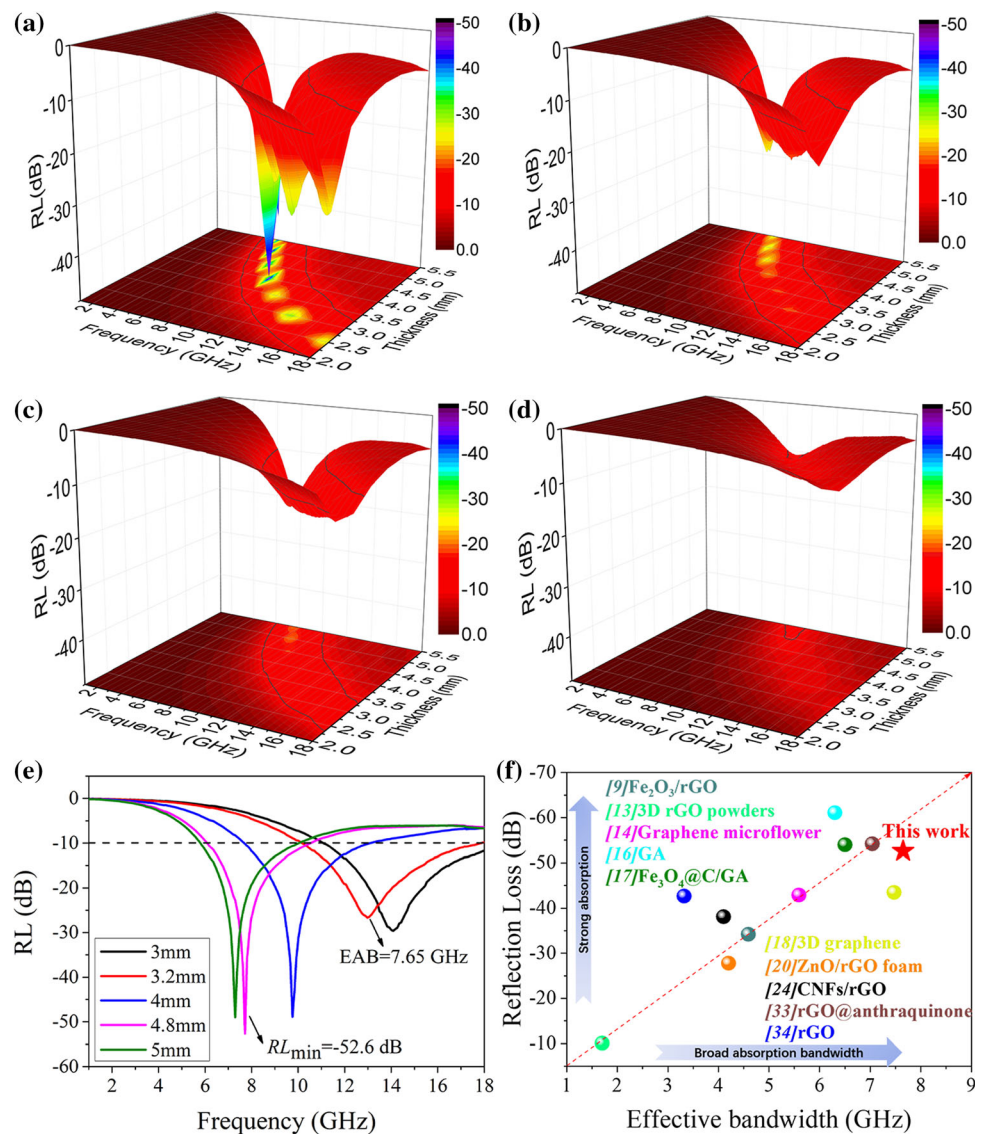


Table 1 Peaks of reflection loss and effective absorption bandwidth with different thicknesses for hGAs

Samples	RL_{min}/dB	EAB/GHz
hGAW	− 10.2 (5 mm)	0.76 (5 mm)
hGA3	− 19.9 (5 mm)	5.5 (4 mm)
hGA2	− 26.8 (5 mm)	5.9 (4 mm)
hGA1	− 49.0 (5 mm)	6.9 (3 mm)

matching model [48], the RL value of absorber can reach the minimum when peak frequency (f_m) and matching thickness (d_m) can meet the following equation

$$d_m = \frac{nc}{4f_m \sqrt{|\epsilon_r||\mu_r|}} (n = 1, 3, 5, \dots). \quad (4)$$

At that particular thickness, the incident wave and reflected wave are out of phase by 180°, leading to counteraction between them at the air–material interface [9, 48]. Obviously, f_m is inversely proportional to d_m for specific electromagnetic parameters, and the RL curves of hGA1 follow this principle well (Fig. 10a). Moreover, the experiment results (d_{exp}) are basically consistent with the simulated curve of d_m calculated according to Eq. 4 (Fig. 10b). These results show that the hGAs conform to the quarter-wavelength matching model well, and the position of f_m can be changed by simply adjusting the thickness.

The impedance of material with good absorption performance should be close to the free space so that more EM wave can enter the material. The impedance matching ratio Z ($Z = |Z_{in}/Z_0|$) is usually used to evaluate this property of the material. When the value of Z is closer to 1, it indicates that the material can achieve better impedance matching. Figure 10c shows the frequency dependence of Z values for hGA1 at different thicknesses. Combined with Fig. 10a, it can be found that the Z values at f_m with different thicknesses are all close to 1. Thus, it can be seen that impedance matching of the material is pivotal to its EM wave absorption ability.

The impedance matching of different hGAs was investigated. Z value contour maps of aerogels at different thicknesses are presented in Fig. 11. As it can be seen that the area near $Z = 1$ is shown with black diagonal lines, and its size is closely related to the concentration of ethanol. Obviously, the obtained hGA1, which possesses lower density and higher permittivity, exhibits a larger area than others,

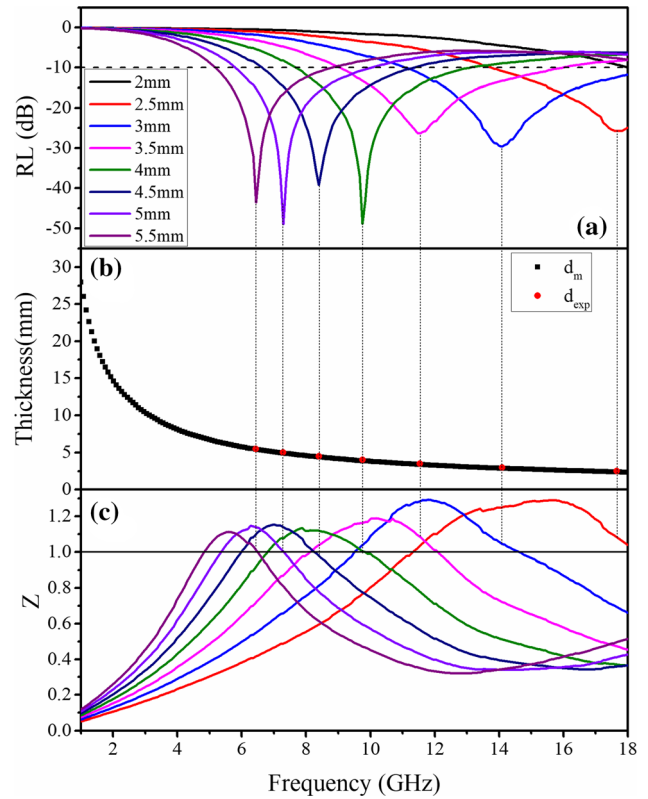


Figure 10 a Reflection loss of hGA1 with different thicknesses. b Calculated matching thicknesses d_m under $n = 11$ versus the d_{exp} obtained from Fig. 10a. c Impedance matching characteristics of hGA1.

suggesting its better impedance matching characteristic. In addition, from Fig. 11a–d, the area with black diagonal lines moves downward in the high-frequency range, revealing the gradually reduced matching thickness of hGAs, which is consistent with the quarter-wavelength matching model.

Based on the above discussions, the hGA1 prepared through the ethanol-assisted hydrothermal method followed by heat treatment shows excellent EM wave absorption performance, which is caused by many reasons.

First, the process of preparing GO into hGA by hydrothermal and heat treatment will reduce GO partially. The restoration of the conjugated structure of hGAs can promote the motion of charge carriers under the alternating electromagnetic field and increase micro-current [49], thus consuming electromagnetic energy. According to Fig. 7d, the conductivity of hGA1 and hGA2, which are prepared with more ethanol, is higher than others significantly, demonstrating their stronger conductive loss.

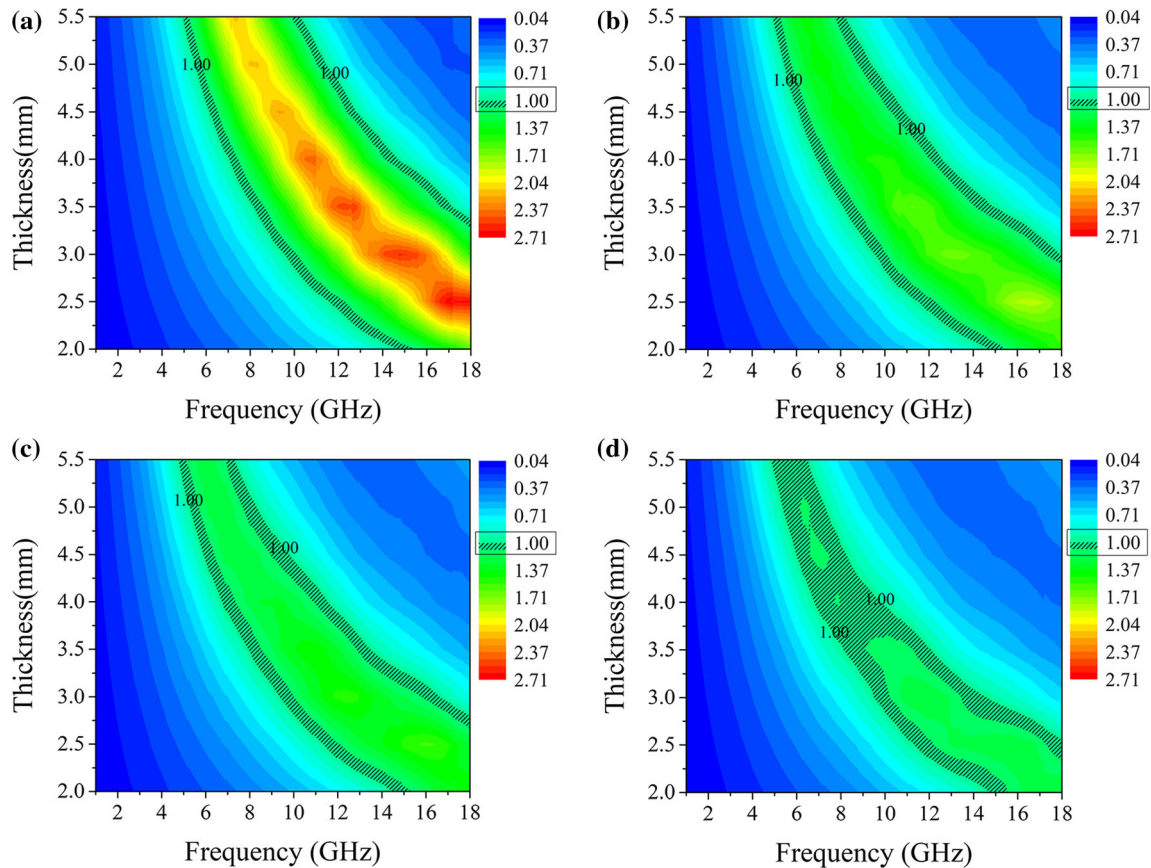


Figure 11 Contour map of the impedance matching ratio for **a** hGAW, **b** hGA3, **c** hGA2, and **d** hGA1.

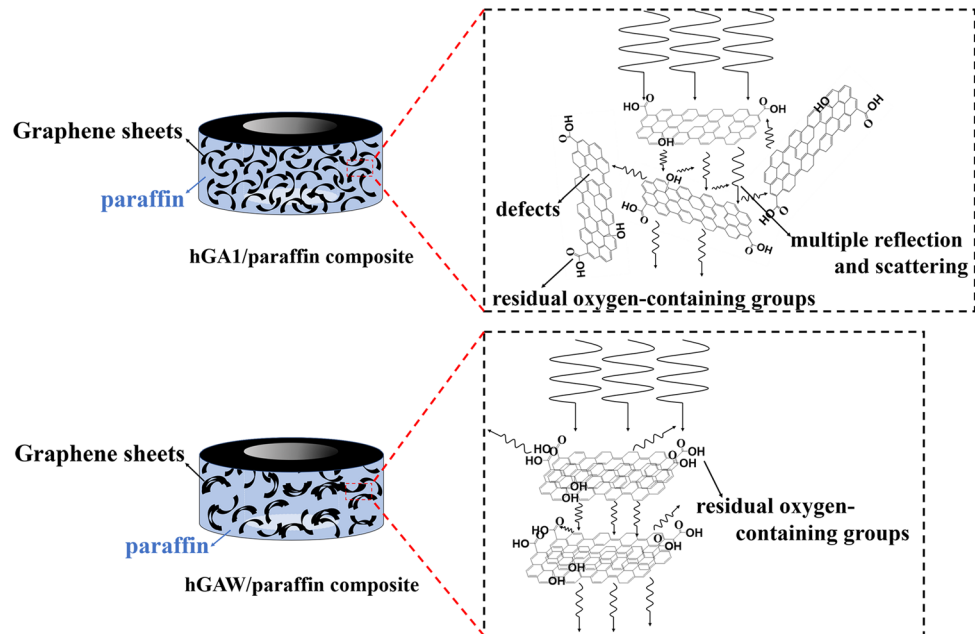
Second, the temperature used during the heat treatment process is only 300 °C, which can retain a certain amount of oxygen-containing functional groups in hGAs. Under the alternating electromagnetic field, the residual C–O and C=O can lead to electric dipole polarization due to the different abilities to catch electrons between carbon and oxygen atoms. At the same time, the defects can act as polarization centers to generate polarization relaxation, which is favorable to the attenuation of EM wave [20, 45]. Besides, the morphologies of hGAs are diverse due to their different amounts of ethanol used during preparation. Using more ethanol can effectively inhibit the agglomeration of graphene sheets, thereby increasing the dangling oxygen-containing bonds and the exposed defects and promoting the polarization effect.

Besides, due to the thin and wrinkled graphene sheets, along with the porous internal structure, hGA1 could readily disperse in the paraffin matrix uniformly [50, 51]. Dispersion of the absorber in the matrix is significant for its performance. As

illustrated in Fig. 12, good dispersion contributes to the multiple reflections and scattering of EM wave entered the interior. Beyond that, the transmission of micro-currents under the applied electric field, as well as the formation of interfaces between the absorber and matrix [38] also largely rely on the uniform distribution of the absorber. So enhanced conductive loss, multiple reflections, and heterogeneous interfacial relaxation caused by the mechanisms mentioned above can also lead to the excellent absorption performance of hGA1.

In addition to attenuation ability, the impedance matching of materials is another critical factor affecting their performance. In this paper, the suitable degree of reduction and ultralow filler content can help regulate the conductivity of hGA/paraffin composites, and then, good impedance matching can be obtained for EM wave absorption. Furthermore, thin and wrinkled graphene sheets and their homogeneous dispersion can reduce the reflection of incident EM wave at the air–material interface, making the impedance of hGA1 much closer to that of the

Figure 12 Schematic diagram of different propagation processes of EM wave in hGA1/paraffin composite and hGAW/paraffin composite.



free space [18]. Thus, more EM wave can enter the interior of the aerogel.

Conclusions

In summary, a series of ultralight graphene aerogels were successfully synthesized by the ethanol-assisted hydrothermal method using graphene oxide as the raw material and EtOH/H₂O as the solvent. By varying the volume ratio of EtOH/H₂O, the microstructures of the graphene aerogels can be easily tuned. SEM results indicate that the introduction of ethanol greatly inhibits the clumping of graphene sheets and reduces the volume shrinkage of the aerogel. For the optimized EtOH/H₂O of 1:1, the obtained hGA1 with 3 wt% filler content can reach the RL_{\min} and EAB of -52.6 dB at 4.8 mm and 7.65 GHz at 3.2 mm, respectively. Analyses reveal that the proper level of reduction and the homogeneous dispersion in the matrix may be account for the excellent EM absorption properties of this material. Considering the great compatibility and excellent absorption performance, it is believed that such graphene-based EAM prepared through this facile synthesis strategy can serve as an effective component for lightweight EM absorption coating-related fields.

Acknowledgements

The authors acknowledge the Beijing Municipal Science and Technology Project (Z161100002116029) for financial support.

Declarations

Conflict of interest There are no conflicts to declare.

References

- [1] Sultanov F, Daulbayev C, Bakbolat B, Daulbayev O (2020) Advances of 3D graphene and its composites in the field of microwave absorption. *Adv Colloid Interface Sci* 285:102281. <https://doi.org/10.1016/j.cis.2020.102281>
- [2] Cao MS, Han C, Wang XX, Zhang M, Zhang YL, Shu JC, Yang HJ, Fang XY, Yuan J (2018) Graphene nanohybrids: excellent electromagnetic properties for the absorbing and shielding of electromagnetic waves. *J Mater Chem C* 6(17):4586–4602. <https://doi.org/10.1039/c7tc05869a>
- [3] Huang L, Chen C, Li Z, Zhang Y, Zhang H, Lu J, Ruan S, Zeng YJ (2020) Challenges and future perspectives on microwave absorption based on two-dimensional materials and structures. *Nanotechnology* 31(16):162001. <https://doi.org/10.1088/1361-6528/ab50af>
- [4] Shi KZ, Li J, Wu Y, Bai H, Hong Y, Zhou ZX (2019) Lightweight composite microwave absorbing materials based on graphene aerogels with honeycomb structure. *Phys*

- Status Solidi-Rapid Res Lett 13(8):1900179. <https://doi.org/10.1002/pssr.201900179>
- [5] Li JS, Huang H, Zhou YJ, Zhang CY, Li ZT (2017) Research progress of graphene-based microwave absorbing materials in the last decade. *J Mater Res* 32(7):1213–1230. <https://doi.org/10.1557/jmr.2017.80>
- [6] Li Q, Zhang Z, Qi L, Liao Q, Kang Z, Zhang Y (2019) Toward the application of high frequency electromagnetic wave absorption by carbon nanostructures. *Adv Sci* 6(8):1801057. <https://doi.org/10.1002/advs.201801057>
- [7] Chen H, Ma W, Huang Z, Zhang Y, Huang Y, Chen Y (2019) Graphene-based materials toward microwave and terahertz absorbing stealth technologies. *Adv Opt Mater* 7(8):1801318. <https://doi.org/10.1002/adom.201801318>
- [8] Wang YF, Chen DL, Yin X, Xu P, Wu F, He M (2015) Hybrid of MoS₂ and reduced graphene oxide: a lightweight and broadband electromagnetic wave absorber. *ACS Appl Mater Interfaces* 7(47):26226–26234. <https://doi.org/10.1021/acsami.5b08410>
- [9] Wang S, Jiao Q, Liu X, Xu Y, Shi Q, Yue S, Zhao Y, Liu H, Feng C, Shi D (2019) Controllable synthesis of γ -Fe₂O₃ nanotube/porous rGO composites and their enhanced microwave absorption properties. *ACS Sustain Chem Eng* 7(7):7004–7013. <https://doi.org/10.1021/acssuschemeng.8b06729>
- [10] Ma JN, Liu W, Quan B, Liang XH, Ji GB (2017) Incorporation of the polarization point on the graphene aerogel to achieve strong dielectric loss behavior. *J Colloid Interface Sci* 504:479–484. <https://doi.org/10.1016/j.jcis.2017.06.004>
- [11] Lv H, Guo Y, Zhao Y, Zhang H, Zhang B, Ji G, Xu ZJ (2016) Achieving tunable electromagnetic absorber via graphene/carbon sphere composites. *Carbon* 110:130–137. <https://doi.org/10.1016/j.carbon.2016.09.009>
- [12] Liu J, Duan Y, Song L, Hu J, Zeng Y (2019) Heterogeneous nucleation promoting formation and enhancing microwave absorption properties in hierarchical sandwich-like polyaniline/graphene oxide induced by mechanical agitation. *Compos Sci Technol* 182:107780. <https://doi.org/10.1016/j.compscitech.2019.107780>
- [13] Liang L, Yang R, Han G, Feng Y, Zhao B, Zhang R, Wang Y, Liu C (2019) Enhanced electromagnetic wave-absorbing performance of magnetic nanoparticles-anchored 2D Ti₃C₂T_x MXene. *ACS Appl Mater Interfaces* 12(2):2644–2654. <https://doi.org/10.1021/acsami.9b18504>
- [14] Liang L, Li Q, Yan X, Feng Y, Wang Y, Zhang H-B, Zhou X, Liu C, Shen C, Xie X (2021) Multifunctional magnetic Ti₃C₂T_x MXene/Graphene aerogel with superior electromagnetic wave absorption performance. *ACS Nano* 15(4):6622–6632. <https://doi.org/10.1021/acsnano.0c09982>
- [15] Liang L, Li Z, Bai Z, Feng Y, Guo X, Ma J, Liu C (2021) Dependence of electromagnetic wave absorption properties on the topography of Ni anchoring on reduced graphene oxide. *Chin Chem Lett* 32(2):870–874. <https://doi.org/10.1016/j.ccllet.2020.06.014>
- [16] Fang S, Huang D, Lv R, Bai Y, Huang Z-H, Gu J, Kang F (2017) Three-dimensional reduced graphene oxide powder for efficient microwave absorption in the S-band (2–4 GHz). *RSC Adv* 7(41):25773–25779. <https://doi.org/10.1039/c7ra03215c>
- [17] Chen C, Xi J, Zhou E, Peng L, Chen Z, Gao C (2018) Porous graphene microflowers for high-performance microwave absorption. *Nanomicro Lett* 10(2):26. <https://doi.org/10.1007/s40820-017-0179-8>
- [18] Zhang Y, Huang Y, Zhang T, Chang H, Xiao P, Chen H, Huang Z, Chen Y (2015) Broadband and tunable high-performance microwave absorption of an ultralight and highly compressible graphene foam. *Adv Mater* 27(12):2049–2053. <https://doi.org/10.1002/adma.201405788>
- [19] Wang ZC, Wei RB, Gu JW, Liu H, Liu CT, Luo CJ, Kong J, Shao Q, Wang N, Guo ZH, Liu XB (2018) Ultralight, highly compressible and fire-retardant graphene aerogel with self-adjustable electromagnetic wave absorption. *Carbon* 139:1126–1135. <https://doi.org/10.1016/j.carbon.2018.08.014>
- [20] Liu WW, Li H, Zeng QP, Duan HN, Guo YP, Liu XF, Sun CY, Liu HZ (2015) Fabrication of ultralight three-dimensional graphene networks with strong electromagnetic wave absorption properties. *J Mater Chem A* 3(7):3739–3747. <https://doi.org/10.1039/c4ta06091a>
- [21] Ma J, Li W, Fan Y, Yang J, Yang Q, Wang J, Luo W, Zhou W, Nomura N, Wang L, Jiang W (2019) Ultrathin and lightweight graphene aerogel with precisely tunable density for highly efficient microwave absorbing. *ACS Appl Mater Interfaces* 11(49):46386–46396. <https://doi.org/10.1021/acsaami.9b17849>
- [22] Cheraghi Bidsorkhi H, D'Aloia AG, Tamburrano A, De Bellis G, Delfini A, Ballirano P, Sarto MS (2019) 3D porous graphene based aerogel for electromagnetic applications. *Sci Rep* 9(1):15719. <https://doi.org/10.1038/s41598-019-52230-5>
- [23] Lv H, Li Y, Jia Z, Wang L, Guo X, Zhao B, Zhang R (2020) Exceptionally porous three-dimensional architectural nanostructure derived from CNTs/graphene aerogel towards the ultra-wideband EM absorption. *Compos B Eng* 196:108122. <https://doi.org/10.1016/j.compositesb.2020.108122>
- [24] Yang C, Hao S-J, Dai S-L, Zhang X-Y (2017) Nanocomposites of poly(vinylidene fluoride) - controllable hydroxylated/carboxylated graphene with enhanced dielectric

- performance for large energy density capacitor. *Carbon* 117:301–312. <https://doi.org/10.1016/j.carbon.2017.03.004>
- [25] Chen HH, Huang ZY, Huang Y, Zhang Y, Ge Z, Qin B, Liu ZF, Shi Q, Xiao PS, Yang Y, Zhang TF, Chen YS (2017) Synergistically assembled MWCNT/graphene foam with highly efficient microwave absorption in both C and X bands. *Carbon* 124:506–514. <https://doi.org/10.1016/j.carbon.2017.09.007>
- [26] Zhang P, Li J, Lv L, Zhao Y, Qu L (2017) Vertically aligned graphene sheets membrane for highly efficient solar thermal generation of clean water. *ACS Nano* 11(5):5087–5093. <https://doi.org/10.1021/acsnano.7b01965>
- [27] Zhang J, Yang H, Shen G, Cheng P, Zhang J, Guo S (2010) Reduction of graphene oxide via L-ascorbic acid. *Chem Commun (Camb)* 46(7):1112–1114. <https://doi.org/10.1039/b917705a>
- [28] Tian J, Yang J, Yang C, Hao S (2019) Compression and reduction of graphene oxide aerogels into flexible, porous and functional graphene films. *J Mater Sci* 54(20):13147–13156. <https://doi.org/10.1007/s10853-019-03828-7>
- [29] Zhang X, Wang J, Su X, Huo S (2019) Facile synthesis of reduced graphene oxide-wrapped CNFs with controllable chemical reduction degree for enhanced microwave absorption performance. *J Colloid Interface Sci* 553:402–408. <https://doi.org/10.1016/j.jcis.2019.06.055>
- [30] Zhang Y, Huang Y, Chen HH, Huang ZY, Yang Y, Xiao PS, Zhou Y, Chen YS (2016) Composition and structure control of ultralight graphene foam for high-performance microwave absorption. *Carbon* 105:438–447. <https://doi.org/10.1016/j.carbon.2016.04.070>
- [31] Mahadik DB, Lee YK, Park C-S, Chung H-Y, Hong M-H, Jung H-N-R, Han W, Park H-H (2015) Effect of water ethanol solvents mixture on textural and gas sensing properties of tin oxide prepared using epoxide-assisted sol-gel process and dried at ambient pressure. *Solid State Sci* 50:1–8. <https://doi.org/10.1016/j.solidstatesciences.2015.10.003>
- [32] Paredes JI, Villar-Rodil S, Martinez-Alonso A, Tascon JM (2008) Graphene oxide dispersions in organic solvents. *Langmuir* 24(19):10560–10564. <https://doi.org/10.1021/la801744a>
- [33] Liu Y, Yuan G, Jiang Z, Yao Z, Yue M (2014) Solvothermal synthesis of graphene nanosheets as the electrode materials for supercapacitors. *Ionics* 21(3):801–808. <https://doi.org/10.1007/s11581-014-1222-0>
- [34] Liu YF, Yuan GH, Jiang ZH, Yao ZP (2014) Solvothermal synthesis of Mn₃O₄ nanoparticle/graphene sheet composites and their supercapacitive properties. *J Nanomater* 2014:1–11. <https://doi.org/10.1155/2014/190529>
- [35] Song CQ, Yin XW, Han MK, Li XL, Hou ZX, Zhang LT, Cheng LF (2017) Three-dimensional reduced graphene oxide foam modified with ZnO nanowires for enhanced microwave absorption properties. *Carbon* 116:50–58. <https://doi.org/10.1016/j.carbon.2017.01.077>
- [36] Zhou C, Geng S, Xu X, Wang T, Zhang L, Tian X, Yang F, Yang H, Li Y (2016) Lightweight hollow carbon nanospheres with tunable sizes towards enhancement in microwave absorption. *Carbon* 108:234–241. <https://doi.org/10.1016/j.carbon.2016.07.015>
- [37] Zhang XF, Dong XL, Huang H, Liu YY, Wang WN, Zhu XG, Lv B, Lei JP, Lee CG (2006) Microwave absorption properties of the carbon-coated nickel nanocapsules. *Appl Phys Lett* 89(5):053115. <https://doi.org/10.1063/1.2236965>
- [38] Wang S, Hu K, Huang F, Zhang M, Wu S, Liu Q, Kong X (2019) Activating microwave absorption via noncovalent interactions at the interface based on metal-free graphene nanosheets. *Carbon* 152:818–826. <https://doi.org/10.1016/j.carbon.2019.06.079>
- [39] Liao C, Zhu X, Xie W, Zeng F, Yi S, Cheng H, Kuang J, Deng Y, Cao T (2018) Solvent-assisted thermal reduction of microcrystalline graphene oxide with excellent microwave absorption performance. *RSC Adv* 8(28):15315–15325. <https://doi.org/10.1039/c8ra01764f>
- [40] Sun H, Che R, You X, Jiang Y, Yang Z, Deng J, Qiu L, Peng H (2014) Cross-stacking aligned carbon-nanotube films to tune microwave absorption frequencies and increase absorption intensities. *Adv Mater* 26(48):8120–8125. <https://doi.org/10.1002/adma.201403735>
- [41] Zhuo RF, Qiao L, Feng HT, Chen JT, Yan D, Wu ZG, Yan PX (2008) Microwave absorption properties and the isotropic antenna mechanism of ZnO nanotrees. *J Appl Phys* 104(9):094101. <https://doi.org/10.1063/1.2973198>
- [42] Sun X, He JP, Li GX, Tang J, Wang T, Guo YX, Xue HR (2013) Laminated magnetic graphene with enhanced electromagnetic wave absorption properties. *J Mater Chem C* 1(4):765–777. <https://doi.org/10.1039/c2tc00159d>
- [43] Frenkel J, Dorfman J (1930) Spontaneous and induced magnetisation in ferromagnetic bodies. *Nature* 126(3173):274–275. <https://doi.org/10.1038/126274a0>
- [44] Yu H, Wang T, Wen B, Lu M, Xu Z, Zhu C, Chen Y, Xue X, Sun C, Cao M (2012) Graphene/polyaniline nanorod arrays: synthesis and excellent electromagnetic absorption properties. *J Mater Chem* 22(40):21679–21685. <https://doi.org/10.1039/c2jm34273a>
- [45] Wang C, Han XJ, Xu P, Zhang XL, Du YC, Hu SR, Wang JY, Wang XH (2011) The electromagnetic property of chemically reduced graphene oxide and its application as microwave absorbing material. *Appl Phys Lett* 98(7):072906. <https://doi.org/10.1063/1.3555436>

- [46] Xu J, Sun L, Qi X, Wang Z, Fu Q, Pan C (2019) A novel strategy to enhance the multiple interface effect using amorphous carbon packaged hydrogenated TiO₂ for stable and effective microwave absorption. *J Mater Chem C* 7(20):6152–6160. <https://doi.org/10.1039/c9tc00483a>
- [47] Ks S, Js B, Gk I, Ck K, Kj M, Ck S (1991) Complex permeability and permittivity and microwave absorption of ferrite-rubber composite in X-band frequencies. *IEEE Trans Magn* 27(6):5462–5464. <https://doi.org/10.1109/20.278872>
- [48] Yusoff AN, Abdullah MH, Ahmad SH, Jusoh SF, Mansor AA, Hamid SAA (2002) Electromagnetic and absorption properties of some microwave absorbers. *J Appl Phys* 92(2):876–882. <https://doi.org/10.1063/1.1489092>
- [49] Cheng Y, Li Z, Li Y, Dai S, Ji G, Zhao H, Cao J, Du Y (2018) Rationally regulating complex dielectric parameters of mesoporous carbon hollow spheres to carry out efficient microwave absorption. *Carbon* 127:643–652. <https://doi.org/10.1016/j.carbon.2017.11.055>
- [50] Zhan W, Fu X, Wang F, Zhang W, Bai G, Xiao W, Zhou A, Sui G, Yang X (2020) Effect of aromatic amine modified graphene aerogel on the curing kinetics and interfacial interaction of epoxy composites. *J Mater Sci* 55(24):10558–10571. <https://doi.org/10.1007/s10853-020-04746-9>
- [51] Han NM, Wang Z, Shen X, Wu Y, Liu X, Zheng Q, Kim T-H, Yang J, Kim J-K (2018) Graphene size-dependent multifunctional properties of unidirectional graphene aerogel/epoxy nanocomposites. *ACS Appl Mater Interfaces* 10(7):6580–6592. <https://doi.org/10.1021/acsami.7b19069>

Publisher's Note Springer Nature remains neutral with regard to jurisdictional claims in published maps and institutional affiliations.